Title

Hybrid photoelectrochemical and photovoltaic cells for simultaneous production of chemical fuels and electrical power

Journal

Nature Materials, 17(12)

ISSN

1476-1122

Authors

Segev, Gideon

Beeman, Jeffrey W

Greenblatt, Jeffery B

et al.

Publication Date

2018-12-01

DOI

10.1038/s41563-018-0198-y

Peer reviewed

nature materials

ARTICLES

https://doi.org/10.1038/s41563-018-0198-y

Hybrid photoelectrochemical and photovoltaic cells for simultaneous production of chemical fuels and electrical power

Gideon Segev[1,2], Jeffrey W. Beeman[1,2], Jeffery B. Greenblatt[2,3,4] and Ian D. Sharp[1,2,5]*

Harnessing solar energy to drive photoelectrochemical reactions is widely studied for sustainable fuel production and versatile energy storage over different timescales. However, the majority of solar photoelectrochemical cells cannot drive the overall photosynthesis reactions without the assistance of an external power source. A device for simultaneous and direct production of renewable fuels and electrical power from sunlight is now proposed. This hybrid photoelectrochemical and photovoltaic device allows tunable control over the branching ratio between two high-value products of solar energy conversion, requires relatively simple modification to existing photovoltaic technologies, and circumvents the photocurrent mismatches that lead to significant loss in tandem photoelectrochemical systems comprising chemically stable photoelectrodes. Our proof-of-concept device is based on a transition metal oxide photoanode monolithically integrated onto silicon that possesses both front- and backside photovoltaic junctions. This integrated assembly drives spontaneous overall water splitting with no external power source, while also producing electricity near the maximum power point of the backside photovoltaic junction. The concept that photogenerated charge carriers can be controllably directed to produce electricity and chemical fuel provides an opportunity to significantly increase the energy return on energy invested in solar fuels systems and can be adapted to a variety of architectures assembled from different materials.

The utilization of solar energy to drive (photo)electrochemical reactions has been widely studied for sustainable fuel production and versatile energy storage over different timescales. However, the majority of solar photoelectrochemical (PEC) cells cannot drive the overall photosynthesis reactions without the assistance of an external power source. To provide added power, PEC cells are often connected to photovoltaic (PV) devices in a tandem arrangement. For example, although the thermodynamic potential for water splitting is 1.23 V, the total photovoltage driving the reaction should be at least 1.5 V because of overpotentials associated with the chemical reactions and polarization losses within devices[1,2]. Thus, the PV and PEC components of the tandem cell are typically stacked electronically and optically in series, thereby yielding the sum of photovoltage contributions from each subcell with maximum light energy utilization. The optimal set of materials required to produce this voltage varies according to many parameters. However, in most cases, a combination of a silicon bottom junction with a wider-bandgap material yields the highest solar to hydrogen conversion efficiency[3] and is also the simplest from a technological standpoint. For this reason, significant efforts have been undertaken to realize water-splitting devices in which a wide-bandgap material, typically a metal oxide, serves as a top junction that is connected to bottom silicon junctions[4–10]. In such configurations the current through the system is determined by the layer exhibiting the lowest performance. This poor performance may be a result of low optical generation in a wide-bandgap material, lossy charge transport in a metal oxide, slow kinetics of the chemical reaction, or a combination of these factors. As a result, nearly all reported devices operate at current densities that are far below the thermodynamic efficiency limit considering the solar energy input and the properties of the individual components in the system[4–8].

Here, we propose a new class of devices, which can be classified as hybrid photoelectrochemical and -voltaic (HPEV) cells. The HPEV cells overcome the problem of mismatched tandem component performance by adding a third electrical terminal to the bottom junction. This third contact allows photogenerated charge carriers that are not consumed by the chemical reaction to be collected as electrical current, thereby producing electrical power at the same time that chemicals are produced. In this work, the functional performance of HPEV devices is validated through finite-element simulations and proof-of-concept HPEV devices are fabricated and tested. To evaluate the broader implications and potential impacts of HPEV devices, overall energy conversion efficiencies are evaluated for a wide range of PEC electrodes operated at different currents and an energy return on energy investment (EROEI) analysis is carried out. We show that, by collecting minority carriers that are not consumed by the chemical reaction as electrical current, electrical power can be harvested at the maximum power point with little effect on the chemical output. As a result, the overall system efficiency increases dramatically: a threefold increase in the overall performance can be achieved using state-of-the-art photoanodes and back-contact solar cells, thereby increasing the EROEI of a prospective 1 GW solar hydrogen plant from 2.3 to above 11.

Coupling losses in PEC energy converters

The Gibbs free energy and overpotentials associated with chemical reactions define a minimum photovoltage that material stacks must generate to drive PEC reactions. Figure 1a illustrates the performance

[1]Chemical Sciences Division, Lawrence Berkeley National Laboratory, Berkeley, CA, USA. [2]Joint Center for Artificial Photosynthesis, Lawrence Berkeley National Laboratory, Berkeley, CA, USA. [3]Energy Analysis and Environmental Impacts Division, , Lawrence Berkeley National Laboratory, Berkeley, CA, USA. [4]Now at Emerging Futures, LLC, Berkeley, CA, USA. [5]Walter Schottky Institut and Physik Department, Technische Universität München, Garching, Germany. *e-mail: sharp@wsi.tum.de

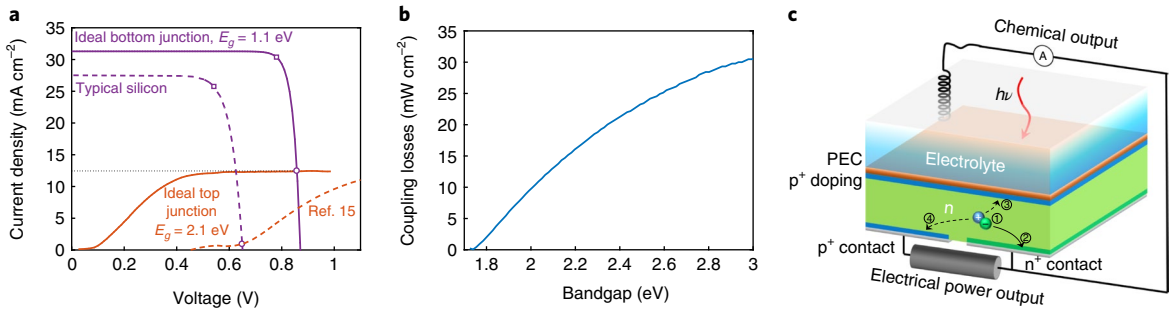

Fig. 1 | Current mismatch losses and the HPEV cell. a, Current–voltage curves of an ideal 2.1 eV bandgap PEC top junction and an ideal 1.1 eV bandgap bottom junction placed behind it (solid lines), as well as a typically performing silicon photovoltaic cell and a TaN (ref. [15]) PEC photoanode (dashed lines) in the same configuration. The silicon solar cell current–voltage characteristics were calculated using a single diode equivalent circuit model as described in Supplementary Section 10. The operating points of the integrated devices are at the intersections of the curves (circles). The maximum power points of the silicon bottom junctions are marked with squares. **b**, Coupling losses in an ideal silicon bottom junction as a function of the bandgap of the top photoelectrode. **c**, Schematic illustration of an HPEV cell.

of a water-splitting device comprising an ideal photovoltaic bottom junction with a bandgap of 1.1 eV located behind a hypothetical PEC top junction. The bandgap of the bottom junction matches that of silicon, and the bandgap of the top PEC junction is 2.1 eV, which is close to the bandgap of widely studied photoanode materials such as haematite[11–14] or Ta_3N_5 (refs. [15–18]). The PEC current–voltage curve illustrates a two-electrode measurement of a photoanode and includes all overpotentials associated with the PEC reaction and the potential drops over the electrolyte. Thus, the operating point of the integrated device is defined by the intersection of the two curves at a current density and voltage of J_{op} and V_{op}, respectively. This point, which is marked by a circle in Fig. 1a, corresponds to a current density of 12.45 mA cm^{-2}, which yields a solar to hydrogen conversion efficiency of 15.3%. However, this operating point is very far from the maximum power point of the bottom junction (square in Fig. 1a), demonstrating severe current mismatches (or coupling losses[19]) and translating to an absolute efficiency loss of 13%. As shown in Fig. 1b, coupling losses rise with increasing top-cell bandgap. This power would be available for extraction but is not collected because of poor integration between the two junctions. Nevertheless, the performance of the top junctions presented in these examples is far above all performance records demonstrated for thin-film photoanodes[12,14,15,20]. This implies that any PEC solar water-splitting system integrated with currently available materials will suffer from dramatically higher current mismatch losses than those of the idealized system represented in Fig. 1a,b. However, this example represents an idealized behaviour, and few materials approach theoretical efficiency limits. To present the performance expectations of modern experimentally demonstrated systems, the dashed curves in Fig. 1a show the current–voltage characteristics of a typical silicon solar cell behind a PEC layer with a bandgap of 2.1 eV (dashed purple curve) and a highly performing TaN photoanode[15] (dashed red curve). The silicon solar cell I–V characteristics were calculated using a single diode equivalent circuit model as described in Supplementary Section 10. The lower photovoltage produced in these two devices brings the current at the operating point to nearly zero. The stark contrast between the relatively high energy conversion efficiencies that can be obtained by the bottom junction and the very low energy conversion efficiencies obtained from corresponding experimental tandem structures highlights the need for addressing practical current mismatch losses. While traditional structures, operated optically and electrically in series, suffer from such limitations, new device concepts offer opportunities for dramatically increasing solar energy conversion efficiencies. Furthermore, novel device architectures may open the door to controllable electricity and fuel production in ways that are inaccessible with conventional structures.

Figure 1c presents an illustration of our proposed HPEV cell. In this example, the bottom junction is made of a three-terminal silicon photovoltaic cell, on top of which the PEC electrode is deposited. The Si cell is bulk-doped n-type and the photoelectrode operates as a photoanode. The electrical coupling layer between the bottom junction and the PEC electrode, as well as underlayers and overlayers, are omitted from Fig. 1c for simplicity. A photocathode-based cell can be made with the opposite doping profiles. The concept underlying the function of the HPEV cell is described in the following. (1) When photons are absorbed in the silicon, electron–hole pairs are generated. (2) As in PV cells, the photogenerated electrons flow to the n$^+$ back contact. Holes have two possible routes: (3) they can flow towards the PEC front contact, from which they will be injected into the PEC layer and participate in the chemical reaction, or (4) they can flow to the second, hole-selective, back contact and contribute to the electrical power output. Hence, the back p$^+$ contact serves as an outlet for holes that are not injected into the top junction and allows for the simultaneous generation of electrical power.

Simulated HPEV device characteristics

In the following, we analyse the functional properties of such an HPEV cell via device simulation, after which we characterize the operational characteristics of an experimentally realized system. The bulk of the three-terminal PV cell of the HPEV device can be viewed as a reservoir of photogenerated charge carriers. Within this reservoir, every charge carrier tends to flow towards the appropriate selective contact and follows the path of least electrical resistance, which is defined by the location at which it was generated and the potential at the contact. Integration of the PV cell with a photoelectrode on its surface couples electrical transport by defining the potential on the top PV junction and imposing the condition for current matching.

To provide insights into how the two photovoltaic junctions are coupled, the current–voltage (J–V) characteristics of the three-terminal Si device are first analysed using finite-element device simulations (see Supplementary Information for simulation details). In particular, the current densities through the front surface (J_{front}) and back surface (J_{back}) p$^+$n junctions are calculated as a function of the voltages V_{front} and V_{back}. Both voltages are defined relative to the common n$^+$ ohmic contact, as indicated in Fig. 2a. The results of the simulations are presented in Fig. 2b, which shows J_{front} and J_{back} as a function of V_{front} for several discrete values of V_{back}. Here, positive current densities indicate that power is passed from the device

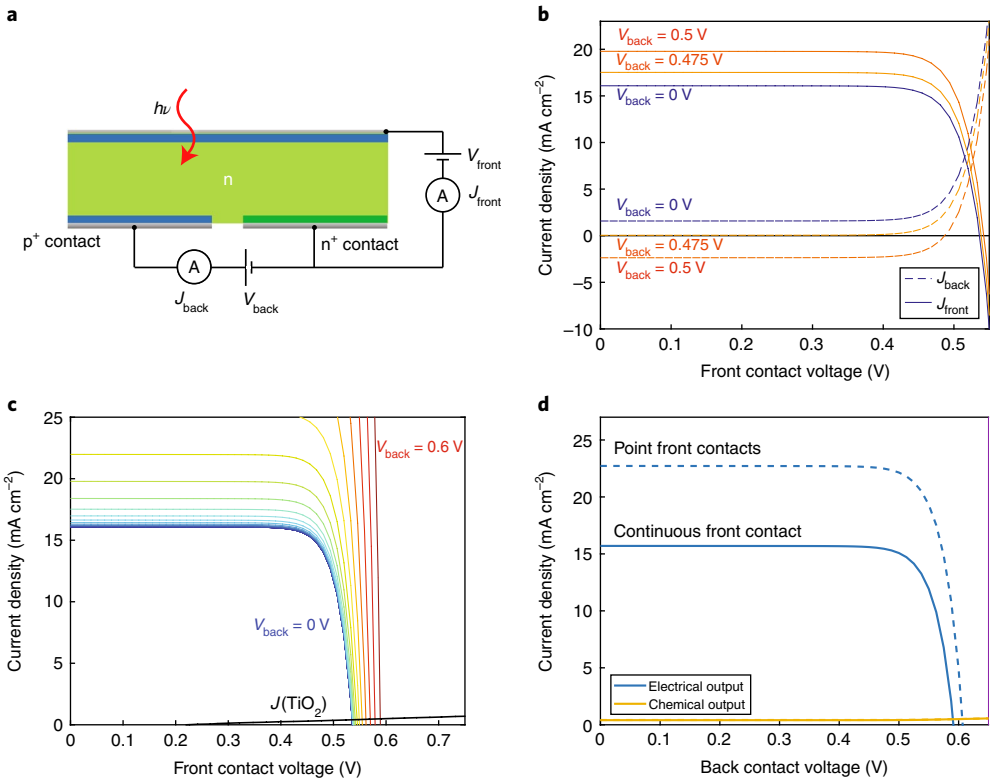

Fig. 2 | Simulated HPEV performance. a, Schematic of the simulated circuit. **b**, Front and back junction currents as a function of front junction voltage and several discrete back junction voltages. **c**, Front contact current for several values of V_{back}. The black curve is the electrochemical load curve of the TiO_2 PEC photoanode[10]. **d**, Electrical and chemical outputs as a function of the back junction voltage. Solid lines are for a continuous top contact and dashed lines are for front surface point contacts. More details on the simulated geometry and material properties are provided in the Supplementary Information.

to the external circuit, and negative current densities indicate that power is passed from the external circuit into the device. From this analysis it is evident that the front and back junctions are electronically coupled, because J_{front} and J_{back} each depend on both V_{front} and V_{back}. Conceptually, this coupling can be understood by recognizing that the photocarriers can be extracted through either of the two p^+n junctions, and the operating points of both junctions define how the photocurrent is partitioned.

To illustrate the coupling between the front and back photovoltaic junctions, we first consider the condition when $V_{back}=0$ V. As shown in Fig. 2b, the front junction is characterized by a standard J–V curve for an illuminated photovoltaic junction. When V_{front} is sufficiently small, J_{front} is within the saturation regime, and most current is extracted across the front junction because of the photogeneration rate and is greater near the front surface. However, as V_{front} approaches the open-circuit voltage, J_{front} decreases and charge collection at the back junction becomes favoured, which results in a corresponding increase in J_{back}. Importantly, this condition is fundamentally different from in a traditional single junction device; instead of all photocarriers recombining when V_{front} is held at open circuit, the carriers in this three-terminal configuration may still be extracted via the back junction. At even larger voltages, when V_{front} exceeds the open-circuit voltage, J_{front} becomes negative and holes are injected from the front contact into the device. In the same way, as V_{back} is varied within the saturation range of J_{back}, there is little influence on the front junction J_{front}–V_{front} characteristics. However, as V_{back} approaches the open-circuit voltage of that junction, J_{back} decreases and J_{front} correspondingly increases. At values of V_{back} larger than the open-circuit voltage, holes are injected from the external circuit into the device.

So far, we have only considered the characteristics of a three-terminal PV cell. However, in the full HPEV device, the front junction of the Si cell is coupled in series to a front surface PEC junction, and current matching between the two defines the common flow of charge across both the top photovoltaic junction and the semiconductor/electrolyte interface. To simulate the performance of a complete spontaneous water-splitting HPEV device, the current density versus electrochemical potential (J–E) curve of a prototypical TiO_2 photoanode, as reported in ref. [10], was used as the electrochemical load. Here, we assume a negligible overpotential for the hydrogen evolution reaction at the counterelectrode (Fig. 1c), such that the electrochemical potential $E=0$ V versus RHE is equivalent to voltage $V=0$ V. Figure 2c shows the PEC load curve defined by the illuminated TiO_2 PEC photoanode along with the previously discussed J_{front}–V_{front} curves for several values of V_{back}.

Figure 2d (solid curves) shows the electrical and chemical outputs as a function of back junction voltage, V_{back}. The electrical output is given by J_{back} and the chemical output is the current density across the semiconductor/electrolyte interface, which defines the reaction rate and is given by the point where the electrochemical load curve meets the top contact current voltage curve, as shown in Fig. 2c. The electrical current extracted from the back junction has little effect on the chemical output. For example, when the back junction voltage corresponds to short circuit, open circuit and at the maximum power point, the chemical output current densities are 0.41, 0.49 and 0.42 mA/cm^{-2}, respectively. Importantly, this means that the chemical output is only weakly dependent on the operating point of the back junction. Such insensitivity can be generalized to any photoanode with a saturation current that is lower than the short-circuit current of the top junction at $V_{back}=0$ as long as the operating point is not near the current onset. In the present case, this means that the back junction can be operated at its maximum power point while only reducing the chemical output by 0.07 mA cm^{-2} relative to its saturation value.

We note that the HPEV cell design presented in Fig. 1c is a conceptual construction that is not yet optimized to achieve the maximum overall combined solar-to-power and solar-to-fuel conversion efficiency. For example, similar to the use of point contacts in high-efficiency silicon solar cells[21,22], localized highly doped regions at the front surface and passivation of the free surfaces can reduce surface recombination losses dramatically. The dashed curves in Fig. 2d describe the performance of an HPEV cell in which the highly doped p^+ region covers narrow 5-μm-wide strips at the front surface instead of being a continuous layer. The removal of lossy, highly doped regions at the front surface increases the back junction electrical output dramatically, yielding a short-circuit current above 22.7 mA cm^{-2}, which accounts for nearly 90% of the photogenerated charge carriers and a maximum extractable power of 11.2 mW cm^{-2}. The reduced recombination also increases the voltage output of the front contacts, which increases the chemical output to 0.44 mA cm^{-2} at the maximum power point. A significant increase in the device performance is also expected by improving the device optics, for example by incorporating back reflectors and a textured front surface, as well as by tuning the photoanode thickness to optimize both anti-reflection and light-harvesting properties. While these opportunities for further optimization of the device geometry and doping profiles are worth highlighting and will be the subject of future work, we focus here on an experimental demonstration of the proof-of-concept HPEV device configuration presented in Fig. 1c.

Experimental validation of the HPEV concept

To validate the HPEV concept and compare its operational characteristics to simulation predictions, physical devices were fabricated and tested. In particular, the experimental realization of HPEV cells was accomplished by deposition of a fluorine-doped tin oxide (FTO) contact layer followed by an n-type TiO_2 photoanode layer on top of a three-terminal Si solar cell, as illustrated in Fig. 1c and described in the Methods. The thickness of the silicon wafer was 0.25 mm, the width of the p^+ and n^+ fingers at its backside was 60 μm, and the spacing between the fingers was 40 μm. The hole diffusion length was estimated to be about 0.14 mm (see Supplementary Section 7 for additional details). The complete HPEV device was then assembled into a custom PEC cell equipped with a quartz glass front window and electrical leads for solid-state photovoltaic measurements, as well as ports for PEC measurements in both two- and three-electrode configurations.

To analyse the characteristics of key junctions within the integrated device, the electrical and chemical outputs were first tested separately. The performance of the HPEV cell for electrical power generation was determined by measuring the *J*–*V* characteristics across the back terminals with the counterelectrode of the PEC cell disconnected. The sample was illuminated with an AM1.5G solar simulator under 1 sun illumination conditions. As described in the Supplementary Information, quantitative analysis of the spectral profile of the solar simulator revealed a reduced ultraviolet intensity relative to the AM1.5G spectrum. A light-emitting diode (LED) was therefore used to compensate for the ultraviolet radiation content. Figure 3a shows the electrical output in the dark, as well as under simulated solar radiation, which is characterized by a short-circuit current density of 3.8 mA cm^{-2}, open-circuit voltage of 0.44 V, and maximum power point voltage of 0.32 V. These results reveal that the back junction qualitatively functions as intended, although there remains significant opportunity for optimization via materials and interface engineering. The rather low power output from the back junction of fabricated devices is primarily a consequence of short minority carrier lifetimes within the n-type Si. Device simulations using a bulk lifetime of 15 μs and a surface recombination velocity of 1,000 cm s^{-1} show an excellent fit to the measured data (Supplementary Fig. 7). A similar Shockley–Read–Hall lifetime for the Czochralski-grown wafers from the same batch was measured via microwave photoconductance decay and was also obtained with spatial collection efficiency extraction[23]. We note that the use of high-quality float-zone (FZ) silicon substrates with millisecond lifetimes, thickness optimization and passivation of free surfaces of the device provides straightforward routes for future efficiency enhancements. Other losses that can be reduced through device optimization include series resistance losses at the metal finger contacts and reduced open-circuit voltage at non-active areas at the device edges. As these issues have already been addressed in commercial back-contact Si solar cells, adoption of such strategies will enable significantly improved HPEV efficiencies in the future.

The PEC characteristics of the HPEV device were tested with the p^+ back contact of the PV junction disconnected (that is, with no electrical power generation). Figure 3b,c show the PEC *J*–*E* curves measured in three- and two-electrode configurations, respectively, in the dark and under simulated 1 sun illumination. In both cases the working electrode was connected to the ohmic n^+ back contact of the HPEV cell. Hence, these curves include the photovoltage generated by the top Si junction, as well under the TiO_2/electrolyte interface. Operation in a three-electrode configuration at 1.23 V versus RHE with simulated 1 sun illumination yielded a current density of 104 μA cm^{-2} (Fig. 3b). More importantly, spontaneous overall water splitting with a current density of 85 μA cm^{-2} was achieved with no external bias in the two-electrode configuration (Fig. 3c). These results provide a basis for analysing the operational characteristics of the complete HPEV device and the effect of operational parameters and junction coupling on both chemical and electrical outputs.

The overall performance of the integrated HPEV device was determined by simultaneously measuring the electrical output and the chemical output arising from spontaneous water splitting as a function of the back junction voltage, V_{back}, as described in the Methods. Figure 3d shows the measured PV and PEC currents densities as a function of V_{back} under 1 sun illumination (bold solid and dashed lines, respectively). As predicted by the simulations, the PEC current is nearly independent of the electrical operating point of the back junction, thus allowing extraction of electrical power at the maximum power point without adversely affecting the PEC output.

To further understand the weak coupling between the front and back junctions, the device characteristics were analysed under several ultraviolet LED intensities, spanning from 40 to 530% of the effective ultraviolet intensity of the AM1.5G spectrum, as shown in the thin solid and dashed lines in Fig. 3d. Because the TiO_2 photoanode is responsible for the current limitation through the front junction, variation of the ultraviolet intensity allows for characterization of how current extraction through the back junction is influenced by charge extraction from the front surface. As expected, the PEC current density increases with ultraviolet light intensity as a result of larger optical generation in the current-limiting TiO_2 photoanode. However, the increase in PEC current has a minimal effect on the current extracted from the back junction. This behaviour can be understood by recognizing that the trajectories of charge carriers are statistically defined by the path of least electrical resistance. As such, the PEC current is primarily driven by photocarriers that are generated near the top surface of the silicon. However, due to rather fast recombination of carriers in the Si device (see discussion above), the minority carrier diffusion length is short relative to the wafer thickness. Thus, only carriers that are generated near the back surface are collected by the back contact. As a result, there is little competition for charge carriers between the front and back junctions. For optimized devices with carrier diffusion lengths matched to the device geometry, stronger coupling between front and back junctions is expected, as described by the simulations presented in the previous section. Even in that scenario, the back junction can be operated near the maximum power point without significantly reducing the chemical output due to the significant current mismatches between the wide-bandgap photoanode and the much

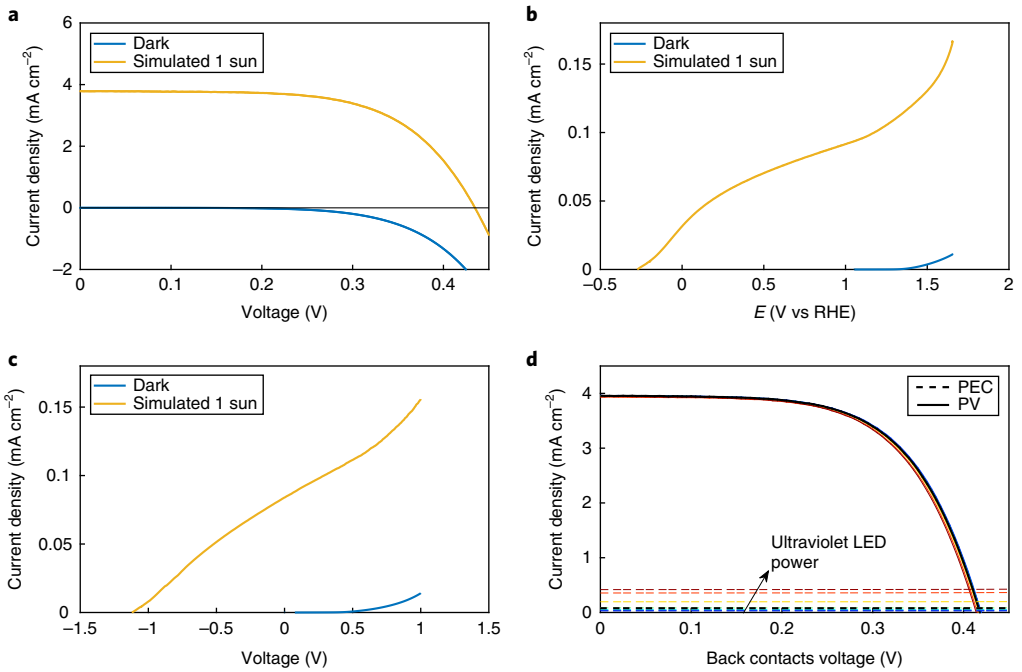

Fig. 3 | HPEV cell characterization. a–c, Electrical (**a**), three-electrode PEC (**b**) and two-electrode PEC (**c**) current–voltage curves in the dark and under 1 sun simulated spectrum. The counterelectrode was disconnected when measuring the electrical performance and the back p^+ contact was disconnected when measuring the PEC performance. **d**, PEC and PV currents as a function of back contacts voltage for several ultraviolet LED power outputs. Black lines are the responses to the 1 sun simulated solar spectrum.

narrower bandgap of Si. For more ideally current-matched HPEV constructions, stronger coupling would emerge and permit the electrical power and chemical outputs to be partitioned on-demand, as described in the next section.

General features of HPEV devices

For the first experimental demonstration of an HPEV cell, we selected TiO_2 as the photoanode because it offers high chemical stability, controllable synthesis, and well-known properties that could be reliably used for simulations. However, the wide bandgap of TiO_2 severely limits its sunlight harvesting capacity, and integration of visible-light-absorbing photoelectrodes into HPEV cells is the ultimate aim. Therefore, we developed and applied an equivalent circuit model to evaluate the optimum bandgap combinations and determine the resulting chemical and electrical outputs. As described in the Supplementary Information, this model assumes strong coupling between the front and back Si junctions arising from minority carrier diffusion lengths that are well matched to the device dimensions. In such a case, charge carriers are partitioned between the front and back junctions such that an equivalent circuit of a simple solar cell can describe the HPEV back-junction output. The short-circuit current of the back junction, reduced by the PEC current, is the overall current that is available for collection and electrical power generation.

To evaluate the key performance metrics for Si-based HPEV cells, the back-junction J–V curves and corresponding power output were calculated as a function of the bandgap of the semiconductor photoelectrode integrated on the front surface, which defines the spectral excitation of the underlying Si, and the extracted PEC current density, which defines the current available for electrical power generation. The Si PV cell parameters were based on the J–V characteristics and external quantum efficiency (EQE) data reported in ref. [22], which represents the performance of modern back-contact Si solar cells. Figure 4a,b show the calculated electrical power output from the back junction of the HPEV cell and the total system efficiency[24] as a function of the top junction current density and bandgap, respectively. The white regions in the upper right sides of the plots represent PEC current densities that cannot be reached considering the bandgaps of the photoelectrodes and the solar spectrum. The white regions in the upper left regions of the plots are defined by PEC currents that are limited by low photogeneration in the Si, which is illuminated through the photoelectrode. As expected, the electrical power output from the back junction is reduced as the PEC current is increased and the PEC bandgap is reduced.

The apex of Fig. 4 represents the ideal photoelectrode bandgap (1.8 eV) for integration on top of a back-junction Si solar cell. Such a device would maximize the chemical output and compares well with multiple publications that have addressed ideal two-terminal tandem structures for PEC water splitting under different assumptions[3,25,26]. However, it is essential to recognize that only a limited set of semiconductor photoelectrodes are actually available. Thus, while optimum bandgap combinations can be predicted, they cannot be practically realized unless new materials are discovered. The HPEV device overcomes this limitation by allowing extraction of excess photogenerated charge carriers as electrical power. This feature is illustrated by the star in Fig. 4, which corresponds to the high-performance $BiVO_4$ layer previously published in ref. [20]. This photoelectrode was reported to have a bandgap of 2.4 eV and is capable of generating a current density of 5.57 mA cm^{-2} at the intersection between the PEC and Si solar cell J–V curves. This chemical output yields a solar-to-hydrogen conversion efficiency of 6.85%, which is the total efficiency for the traditional tandem architecture. However, in an HPEV cell, the simultaneous back-contact power output could reach 13.3 mW cm^{-2}. The result is a total solar energy conversion efficiency of 20.2%.

An EROEI analysis can be used to estimate the overall environmental impact of a renewable energy technology. A 10% solar-to-hydrogen efficient $BiVO_4$ top photoelectrode coupled to a standard silicon absorber is estimated to have an EROEI of 2.34

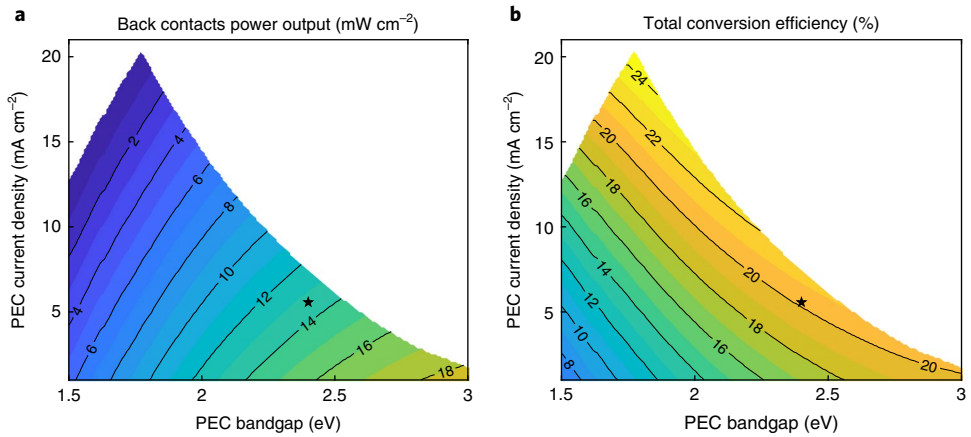

Fig. 4 | Equivalent circuit analysis of HPEV cells. a,**b**, HPEV electrical power output (**a**) and total efficiency (**b**) as a function of the PEC route current and photocatalyst-layer bandgap. The star marks the $BiVO_4$ layer performance reported in ref. [20].

(Supplementary Section 12). Thus, throughout its lifespan, such a solar hydrogen plant will produce 2.34 times the energy required to produce and operate it. The advantage of electricity production in HPEV-based systems is twofold. On top of the electricity exported from the plant, some of the electricity produced can be used to run peripheral systems such as compressors and sensors required for its daily operation, reducing its overall energy inputs. As a result, the EROEI can increase to between 11.66 and 16.16 depending on how the contributions of electricity and hydrogen are added (Supplementary Section 13).

The interdependence of the chemical and electrical outputs in optimally designed HPEV cells may provide means for flexible, real-time outputs partitioned according to demand. For example, in the case of a high demand for electricity, the chemical output can be easily reduced, thereby increasing the current that can be harvested as electrical power. As shown in Fig. 2b,c, power can also be injected from the back contacts into the device, raising the current and voltage at the front surface. To achieve a high flexibility in the chemical output, the electrochemical load curve should have a high slope at its intersection with the silicon front-contact current–voltage curve. While the electrochemical load curves presented in this work are fairly flat at this potential range, applications with other PEC reactions may benefit significantly from this degree of freedom.

The HPEV cell described in this work represents one possible approach for integrating photovoltaic and PEC systems with the goal to reduce current mismatch losses. Several other approaches can be imagined, each with its own specific advantages and limitations. For example, the bottom junction of dual-bandgap systems can be mechanically divided such that one part produces the current required to support the photoelectrochemistry while the other is used to generate electrical power. This type of arrangement can be fabricated by mechanically separating the bottom junction or by having two separated contact grids. While such a configuration might be simpler to fabricate, this comes at the cost of reduced flexibility in operation. In another approach, if the device produces sufficient photovoltage, an electrical load can be connected between the cathode and anode to harvest the extra photovoltage as electricity. While nearly all modern PEC systems generate less photovoltage than desired and none provide excess photovoltage, such a configuration could be applicable to multijunction solar cells, which produce voltages higher than required by the chemical reaction. An elaborated analysis of both conventional and newly imagined architectures is of great interest and is left for future investigation.

Conclusion

A new class of devices, HPEV cells, has been proposed. These devices are three-terminal cells in which a second junction is added to extract charge carriers that cannot be injected into the top junction due to current mismatches. The functional performance of the cells was studied with finite-element modelling and verified in prototypes fabricated from a silicon bottom junction and a TiO_2 top junction. It is shown that charge carriers that do not contribute to the chemical reaction can be harvested as electrical power at the maximum power point with a negligible effect on the chemical output. Equivalent-circuit-based modelling shows that HPEV cells made from off-the-shelf back-contact solar cells can at least double the overall output of the system for top junctions with bandgaps above 2.3 eV. As such, the HPEV device concept could dramatically enhance the energy return on energy invested for PEC systems. The ability to overcome efficiency losses associated with current mismatches provides a route to creating efficient and functional systems from the existing set of materials.

Online content

Any methods, additional references, Nature Research reporting summaries, source data, statements of data availability and associated accession codes are available at https://doi.org/10.1038/s41563-018-0198-y.

Received: 2 June 2018; Accepted: 17 September 2018;
Published online: 29 October 2018

References

1. Bak, T., Nowotny, J., Rekas, M. & Sorrell, C. C. Photo-electrochemical hydrogen generation from water using solar energy. Materials-related aspects. *Int. J. Hydrogen Energy* **27**, 991–1022 (2002).
2. Walter, M. G. et al. Solar water splitting cells. *Chem. Rev.* **110**, 6446–6473 (2010).
3. Hu, S., Xiang, C., Haussener, S., Berger, A. D. & Lewis, N. S. An analysis of the optimal band gaps of light absorbers in integrated tandem photoelectrochemical water-splitting systems. *Energy Environ. Sci.* **6**, 2984–2993 (2013).
4. Liu, C., Tang, J., Chen, H. M., Liu, B. & Yang, P. A fully integrated nanosystem of semiconductor nanowires for direct solar water splitting. *Nano Lett.* **13**, 2989–2992 (2013).
5. Shaner, M. R. et al. Photoelectrochemistry of core–shell tandem junction n–p$^+$-Si/n-WO_3 microwire array photoelectrodes. *Energy Environ. Sci.* **7**, 779–790 (2014).
6. Chakthranont, P., Hellstern, T. R., McEnaney, J. M. & Jaramillo, T. F. Design and fabrication of a precious metal-free tandem core-shell p$^+$n Si/W-doped $BiVO_4$ photoanode for unassisted water splitting. *Adv. Energy Mater.* **7**, 1701515 (2017).

7. Jang, J.-W. et al. Enabling unassisted solar water splitting by iron oxide and silicon. *Nat. Commun.* **6**, 7447 (2015).
8. Abdi, F. F. et al. Efficient solar water splitting by enhanced charge separation in a bismuth vanadate–silicon tandem photoelectrode. *Nat. Commun.* **4**, 2195 (2013).
9. Sheridan, M. V. et al. All-in-one derivatized tandem p+n-silicon-SnO_2/TiO_2 water splitting photoelectrochemical cell. *Nano Lett.* **17**, 2440–2446 (2017).
10. Shaner, M. R., McDowell, M. T., Pien, A., Atwater, H. A. & Lewis, N. S. Si/TiO_2 tandem-junction microwire arrays for unassisted solar-driven water splitting. *J. Electrochem. Soc.* **163**, H261–H264 (2016).
11. Sivula, K., Le Formal, F. & Grätzel, M. Solar water splitting: progress using hematite (α-Fe_2O_3) photoelectrodes. *ChemSusChem* **4**, 432–449 (2011).
12. Warren, S. C. et al. Identifying champion nanostructures for solar water-splitting. *Nat. Mater.* **12**, 842–849 (2013).
13. Tilley, S. D., Cornuz, M., Sivula, K. & Grätzel, M. Light-induced water splitting with hematite: improved nanostructure and iridium oxide catalysis. *Angew. Chem. Int. Ed.* **49**, 6405–6408 (2010).
14. Dotan, H. et al. Resonant light trapping in ultrathin films for water splitting. *Nat. Mater.* **12**, 158–164 (2013).
15. Liu, G. et al. Enabling an integrated tantalum nitride photoanode to approach the theoretical photocurrent limit for solar water splitting. *Energy Environ. Sci.* **9**, 1327–1334 (2016).
16. Takata, T. et al. Visible-light-driven photocatalytic behavior of tantalum-oxynitride and nitride. *Res. Chem. Intermed.* **33**, 13–25 (2007).
17. Li, Y. et al. Vertically aligned Ta_3N_5 nanorod arrays for solar-driven photoelectrochemical water splitting. *Adv. Mater.* **25**, 125–131 (2013).
18. Zhong, M. et al. Highly active GaN-stabilized Ta_3 N_5 thin-film photoanode for solar water oxidation. *Angew. Chem. Int. Ed.* **56**, 4739–4743 (2017).
19. Rothschild, A. & Dotan, H. Beating the efficiency of photovoltaics-powered electrolysis with tandem cell photoelectrolysis. *ACS Energy Lett.* **2**, 45–51 (2016).
20. Pihosh, Y. et al. Photocatalytic generation of hydrogen by core-shell WO_3/$BiVO_4$ nanorods with ultimate water splitting efficiency. *Sci. Rep.* **5**, 11141 (2015).
21. Zhao, J., Wang, A. & Green, Ma 24.5% efficiency silicon PERT cells on tmMCZ substrates and 24.7% efficiency PERL cells on FZ substrates. *Prog. Photovoltaics Res. Appl.* **7**, 471–474 (1999).
22. Mulligan, W. P. et al. in *Proceedings of the 19th EPVSEC* 3–6 (2004).
23. Segev, G. et al. The spatial collection efficiency of charge carriers in photovoltaic and photoelectrochemical cells. *Joule* **2**, 210–224 (2018).
24. Coridan, R. H. et al. Methods for comparing the performance of energy-conversion systems for use in solar fuels and solar electricity generation. *Energy Environ. Sci.* **8**, 2886–2901 (2015).
25. Döscher, H., Geisz, J. F., Deutsch, T. G. & Turner, J. A. Sunlight absorption in water—efficiency and design implications for photoelectrochemical devices. *Energy Environ. Sci.* **7**, 2951–2956 (2014).
26. Bolton, J. R., Strickler, S. J. & Connolly, J. S. Limiting and realizable efficiencies of solar photolysis of water. *Nature* **316**, 495–500 (1985).

Acknowledgements

This material is based on work performed by the Joint Center for Artificial Photosynthesis, a DOE Energy Innovation Hub, supported through the Office of Science of the US Department of Energy under award no. DE-SC0004993. G.S. acknowledges support by the Israeli Ministry of National Infrastructure, Energy and Water Resources under the programme for post-doctoral fellowships.

Author contributions

G.S. and I.D.S. initiated this research. G.S. and J.W.B. fabricated the devices. G.S. carried out the measurements and simulations. J.B.G. conducted the EROEI analysis and wrote the section about it. G.S. and I.D.S. wrote the rest of the manuscript. All authors commented on the manuscript. I.D.S. directed the research.

Competing interests

The authors declare no competing interests.

Additional information

Supplementary information is available for this paper at https://doi.org/10.1038/s41563-018-0198-y.

Reprints and permissions information is available at www.nature.com/reprints.

Correspondence and requests for materials should be addressed to I.D.S.

Publisher's note: Springer Nature remains neutral with regard to jurisdictional claims in published maps and institutional affiliations.

Methods

Device fabrication. The devices used in this study were fabricated using (100)-oriented Czochralski-grown two-side-polished P-doped (2 Ω cm resistivity) Si wafers (0.25 mm thick). The light-incident side of these wafers was ion-implanted with ^{11}B to 3×10^{14} cm^{-2} at 33 keV followed by 5×10^{14} cm^{-2} at 50 keV. This treatment produced a reasonably uniform, metallically doped (5×10^{18} cm^{-3} to 5×10^{19} cm^{-3}) contact region extending 250 nm from the surface into the bulk. The backside of the samples received both n^+ and p^+ implanted contacts in an interleaved comb pattern, as shown in Supplementary Fig. 5. The width of the p^+ and n^+ fingers was 60 μm and the spacing between the fingers was 40 μm. For n^+ ohmic contacts, ^{31}P was implanted to 2×10^{14} cm^{-2} at 33 keV followed by 5×10^{14} cm^{-2} at 75 keV. For backside junction formation, ^{11}B was implanted with the same parameters as for the front surface. After photoresist stripping and oxide removal using an HF vapour etch, the implanted atoms were activated using a 900 °C, 10 s rapid thermal anneal.

Following dopant activation, the Si surface was etched for 1 min in 5% HF and a fluorine-doped tin oxide (FTO) layer was deposited on the top surface using ultrasonic spray pyrolysis (Sono-Tek ExactaCoat) at 500 °C. The precursor used for the depositions was made by mixing 90.2 ml ethanol and 7.23 ml butyltin trichloride with a solution containing 0.122 g ammonium fluoride in 2.46 ml water. The precursor flow rate was 1 ml min^{-1} and the spraying speed was 100 mm s^{-1}. A total of 20 spray repetitions resulted in an FTO layer thickness of about 200 nm (Supplementary Fig. 10).

The TiO_2 PEC layer was deposited on top of the FTO using electron-beam evaporation (Angstrom Engineering, NEXDEP). The deposition was conducted at a substrate temperature of 350 °C and a vacuum pressure of ~10^{-6} torr. The acceleration voltage was set to 7 kV and the deposition rate to 0.5 Å s^{-1}. Post-deposition air annealing was performed at 500 °C for 3.5 h. Supplementary Fig. 13a,b shows plan-view and cross-sectional scanning electron microscopy (SEM) images of the fabricated photoelectrodes. A final photolithographic step and electron-beam evaporation were then used to overlay the backside, comb-patterned ion implants with metal contacts comprising 20 nm of Ti and 300 nm of Au. Following metallization, the wafers were diced into 10 mm × 10 mm chips, each with a single HPEV device as illustrated in Supplementary Fig. 6.

PEC characterization. PEC characterization was conducted using an AAA solar simulator (Oriel Sol3A 94023A) and a 340 nm collimated LED (Thorlabs M340L4 with Thorlabs COP1A collimating optics). The chemical output was measured in 1 M NaOH electrolyte with a Bio-Logic VSP potentiostat in a two-electrode configuration using a platinum wire as counterelectrode or in a three-electrode configuration with a platinum wire counterelectrode and a leak-free Ag/AgCl reference electrode. The electrical output was measured using the second channel of the potentiostat. Simultaneous water-splitting and electric power generation measurements were conducted by connecting each output to a different potentiostat channel and synchronizing the two channels. Linear sweep voltammetry was carried out to measure the electrical output while a two-electrode chronoamperometry measurement at a potential of 0 V versus the reference was used to monitor the chemical output.

EQE measurements. EQE measurements were carried out using a Newport 300 W ozone-free Xe lamp, whose optical output was passed through an Oriel Cornerstone 130 1/8 m monochromator. The sample current was measured with a Gamry Reference 600 potentiostat. The monochromatic light was stepped in 5 nm intervals and chopped at a period between 0.5 and 5 s depending on the settling time of the current signal. A Mightex GCS-6500-15-A0510 LED and a Mightex LGC-019-022-05-V collimator were used to produce the background light bias. Back-junction EQE measurements were conducted with several background light intensities with LED currents of 25, 50, 100, 200 and 400 mA, which correspond to background current densities of 81, 212, 518, 1,150 and 2,350 μA cm^{-2}, respectively. Measurements were also performed without the light bias. The PEC counterelectrode was disconnected during all of these measurements. Front PEC junction EQE measurements were conducted in the two-electrode configuration and in short circuit while the back p^+ was disconnected. The background light bias was applied with an LED current of 500 mA. The photocurrent was calculated by subtracting the current generated under background light illumination from the current generated in the presence of both monochromatic and background light illumination. The incident optical output at each wavelength was measured with a Thorlabs SM05PD2A photodiode. The photodiode was calibrated using a Newport 818-UV/DB calibrated detector.

Data availability

The data that support the findings within this paper are available from the corresponding author upon request.